Solar Energy 287 (2025) 113197

Contents lists available at ScienceDirect

Solar Energy

journal homepage: www.elsevier.com/locate/solener

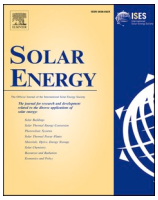

Convection heat loss analysis of a wind-skirted open-cavity tubular receiver for a solar-dish Brayton cycle

Jonathan K. Swanepoel, Willem G. le Roux *, Casey Roosendaal, Jacques Buys

Department of Mechanical and Aeronautical Engineering, University of Pretoria, Private Bag X20, Hatfield 0028, South Africa

ARTICLE INFO

Handling editor: .

Keywords:
Heat loss
Solar thermal
Cavity receiver
Brayton cycle
Tubular receiver
Solar dish

ABSTRACT

Solar-dish Brayton cycle receivers connected to radial turbomachinery usually require large pipe diameters to minimize pressure losses and improve overall cycle performance. However, most convection heat loss correlations in literature are developed for cavity receivers with isothermal assumptions, relatively small pipe diameters, and a unique receiver geometry. The current study therefore compared the similarity of prominent convection heat loss correlations in literature to experimental 5-minute steady-state results from in-field, naturalistic, heat loss testing for a solar-dish Brayton cycle receiver. A large pipe, helically-coiled, open-cavity tubular solar receiver with a wind-skirt was tested. Parametric control was exercised over elevation angles between 22.5° and 90°, average air mass flow rates between 33 g/s and 68 g/s and average inner-cavity temperatures up to 550 °C. Average ambient temperatures ranged from 13 °C to 22 °C and average wind speeds ranged from 0.5 m/s to 3.3 m/s. Results showed that the correlation providing the best fit to the experimental convection heat loss results (with an average difference of 3 %) had the unique ability to account for having a heated coil surface deeper into the cavity.

1. Introduction

Concentrated solar thermal power generation involves the capturing of solar radiation in the form of heat. This can be done by reflecting and concentrating solar radiation towards a heat exchanger or receiver with a working fluid being passed through it. This heat is used to generate electricity through either turbine generators or Stirling engines, or the heat can also be used as a direct source of heating for industrial processes. Several types of solar receivers have been investigated in literature for parabolic dish systems: external receivers, cavity receivers and volumetric receivers [1]. The current study incorporates the use of a helically coiled cavity receiver which reduces convection and radiation heat losses from the pipe surface in comparison to external solar receivers [2]. Air can be used as the working fluid in a dish-Brayton power cycle.

Many studies have been conducted to characterise and optimize the performance of solar cavity receivers. Steinfeld and Schubnell [3] focused on aperture sizing to maximizing radiation heat captured while minimizing radiation heat loss through the aperture. The study found that the optimum operating temperature ranged between 800 K and 1300 K. Harris and Lenz [4] found that forced convection heat losses can be three to four times that of natural convection heat losses for wind speeds exceeding 4.5 m/s and using wind skirts at the aperture can reduce the forced convection heat loss significantly. Xiao et al. [5] performed a numerical simulation on a cylindrical coil cavity receiver with varying geometrical characteristics as well as operating conditions. The study found that larger pipe diameters reduced heat absorption, thermal efficiency, and optical efficiency of the cavity receiver. However, the study by Le Roux et al. [6] showed how large pipe diameters improve overall performance of solar dish-Brayton plants due to the decrease in pressure drop between the compressor and turbine. Jilte et al. [7] conducted numerical simulations of free-forced convection on different shapes of open-cavity receivers for different aperture diameters, wind speeds, receiver inclination angles, cavity temperatures. Decreasing the aperture diameter was found to decrease the convective heat losses for all the cavity shapes. It was found that the conically shaped cavity receiver yielded the lowest convective heat losses. This corresponds to the findings of Daboo et al. [8]. Prakash et al. [9] experimentally quantified convection heat loss from cylindrical open-cavity receivers for cavity temperatures between 50 °C and 300 °C, at varying elevation angles and using water as the working fluid. The study showed that convection heat loss was maximized for head-on wind conditions while side-on winds shielded the cavity which was due to the

* Corresponding author.
E-mail address: willem.leroux@up.ac.za (W.G. le Roux).

https://doi.org/10.1016/j.solener.2024.113197
Received 6 September 2024; Received in revised form 11 November 2024; Accepted 12 December 2024
Available online 23 December 2024

Nomenclature

Symbols

a	Aperture size (m)
A	Area (m^2)
AP	Aperture position (−)
AR	Cavity aspect ratio (−)
D	Diameter (m)
f	Function (−)
F	View factor (−)
Gr	Grashof number (−)
h	Specific enthalpy (J/kg)
$\widehat{h}$	Convection heat transfer coefficient (W/m^2K)
k	Conductivity (W/mK)
L	Length (m)
L	Characteristic length (−)
$\dot{m}$	Mass flow rate (kg/s)
Nu	Nusselt number (−)
P	Pressure (Pa)
Pr	Prandtl number (−)
$\dot{Q}$	Heat transfer (W)
r	Radius (m)
Re	Reynolds number (−)
s	Geometric coefficient (−)
T	Temperature (K)
V	Velocity (m/s)

Subscripts

22.5°	22.5° Elevation angle
45°	45° Elevation angle
67.5°	67.5° Elevation angle
90°	90° Elevation angle
amb	Ambient
ap	Aperture
$ap\perp$	Vertical projection of aperture
c	Characteristic parameter
cav	Cavity
cond	Conduction
conv	Convection
cor	Correlation
cz	Convection zone
*Eq*1	Equation (1)
forced	Forced
head	Head on direction
i	Increment
in	Inlet
j	Increment
max	Maximum
nat	Natural
out	Outlet
p	Planar / projected 2D surface
rad	Radiation
side	Side-on to receiver cavity
th	Thermocouple
tot	Total
tube	Exposed tubing surface
wall	Pipe wall surface

Greek

β	Coefficient of thermal expansion, (1/K)
ε	Emissivity
θ	Elevation angle, (degrees)
μ	Viscosity, (pa.s)
ν	Kinematic viscosity, (m^2/s)
π	Pi
σ	Stefan Boltzmann constant
τ	Diameter ratio

Acronyms

CAD	Computer Aided Design
LPG	Liquid Petroleum Gas

cavity shape. Naturalistic experimental studies have been conducted to characterise the performance of cavity receivers but lack detailed heat loss analyses. Zhu et al. [10] conducted an on-sun experimental analysis of a coiled pipe cavity receiver under naturalistic environmental conditions. The receiver pipe diameter was 14 mm, the cavity diameter was 250 mm, and the cavity height was 456 mm. Receiver thermal efficiencies between 70 % and 82 % were achieved. A proceeding study conducted by Wang et al. [11] on the same receiver cavity achieved a receiver solar thermal efficiency of 60 % at similar inlet temperature conditions.

Small-scale solar-dish Brayton cycles with parabolic dish reflectors in the range of 18 m^2 to 25 m^2 are currently being investigated at the University of Pretoria. Le Roux et al. [12,13] designed and numerically optimised an open-cavity rectangular tubular receiver with a pipe inner diameter of 83.3 mm. It was found that open cavity receivers with larger pipe diameters will perform better in a Brayton cycle with receiver thermal efficiencies of 45 % − 75 % being reported. Le Roux et al. [6,13] manufactured the rectangular open-cavity receiver with a coil pipe outer diameter of 0.0889 m for experimental validation of the earlier numerical study [6]. Results showed a total experimental heat loss rate of 1.7 kW for the receiver with no air gaps and 3.8 kW for the receiver with air gaps between the large coil pipes at an inner-cavity temperature of 590 K. A similar experimental heat loss analysis was done on the rectangular open-cavity receiver where heated process air was passed through the receiver coil. The total heat loss rate from the receiver was found to be 5.6 kW with the receiver at a 90° elevation angle, an inner-cavity temperature of 947 K and an air mass flow rate of 0.053 kg/s [14,15]. Craig et al. [16] developed a CFD model to estimate the heat losses from the open-cavity tubular receiver based on the receiver developed by Le Roux et al. [6]. The study found that 40 % − 50 % of the absorbed heat from the sun was transferred to the HTF for receiver elevation angles ranging from 45° to 90° and wind speeds ranging from 0.5 m/s to 4 m/s for both head-on and back-on winds.

There is currently a lack of empirical research characterizing performance for open-cavity, coiled-pipe receivers with relatively large pipe diameters used in solar-dish Brayton power cycles. Additionally, correlations have usually been developed in controlled lab studies at parameterised wind conditions which do not resemble wind conditions during field testing. Initial experimental studies have recently been conducted on the tubular receiver of Le Roux [13] but did not provide enough detail characterising the heat loss at various cavity temperatures and elevation angles. In the current study, the dish-mounted rectangular open-cavity solar receiver with a large pipe diameter, proposed for a Brayton cycle by Le Roux [13], was therefore further experimentally investigated. A range of cavity temperatures and elevation angles were considered in outdoor controlled tests with no solar exposure and a combustion chamber providing heated air at the receiver inlet (to mimic operation in a small-scale recuperated solar-dish Brayton cycle). Total heat loss from the receiver was found by measuring the inlet and outlet temperatures of the gas. Conduction and radiation heat loss was analytically modelled, and convection heat loss was determined from an energy balance. Convection heat loss results were then compared with

empirical convection heat loss models to enable appropriate modelling of convection heat loss from a large-pipe-diameter cavity receiver for a solar-dish Brayton cycle (solarised micro-turbine) in future studies.

2. Experimental setup

The solar receiver was fixed to the end of a solar tracking system, located on the roof of Engineering Building 2 at the University of Pretoria, South Africa. The solar tracking system was not used to track the sun but to tilt the receiver to a set of elevation angles during testing. The dish (a faceted vacuum membrane reflector [17]) was removed during testing. An air blower supplied air to the rest of the process components at a controlled mass flow rate (see Fig. 1).

The mass flow rate was measured using a mass flow meter located after a calming section. The supply air was passed through the combustion chamber which then heated the air using the combustion of LPG.

2.1. Receiver coil

The solar receiver consisted of an 88.9 mm outer diameter pipe with a 3.05 mm wall thickness (stainless steel 316). The pipe was coiled in a rectangular shape with 6.25 coil rotations (see Fig. 2). The outside of the receiver was covered with ceramic fibre insulation to minimise heat loss. Two flanges were located at the inlet and outlet of the receiver for connecting to the rest of the equipment using high-temperature gaskets. The distance between each coil was between 5 mm and 10 mm allowing enough clearance for thermal expansion. The rectangular shape of the coil was chosen primarily for ease of manufacturing, despite literature showing that rectangular shaped receivers do not have the greatest thermal efficiency [7,8].

2.2. Sensors and thermocouples

Twenty K-type TC40 weld-on thermocouples were distributed along the length of the receiver coil pipe to record the surface temperatures at various positions along the flow path. The thermocouples were welded on the outer cavity, at approximately −50°, in contact with the cavity insulation so that the thermocouple junctions would not be directly influenced by the incoming thermal radiation (see Fig. 3). This was done to get a measurement that better represents the average outer-cavity temperature of the receiver pipe based on the study of Craig et al. [16]. The arrangement and numbering of the weld-on surface thermocouples are shown in Fig. 2 and Fig. 3. Surface thermocouple 6 was the only surface thermocouple positioned on the inner cavity and at approximately 25° to minimise the radiative effect on the temperature measurement from the aperture.

Seven K-type, TC40 3-mm-diameter insert thermocouples were used to measure the temperature of the air flowing through the receiver. Four insert thermocouples were placed at the inlet and three at the outlet of the receiver, arranged as shown in Fig. 4 to obtain an average air temperature at the inlet and outlet of the receiver. A weld-on thermocouple was placed at the same location as the insert thermocouples to obtain the surface temperature. The surface temperature was then used to correct the air temperature reading due to radiation effects between the thermocouple and the coil pipe surface.

2.3. Insulation

50-mm-thick ceramic fibre boards rated for 1250°C were used as insulation material for the receiver [18]. Two panels were used on all four sides of the receiver as well as at the top and bottom forming an insulation thickness of 100 mm around the receiver. A layer of aluminium foil was placed between the 50 mm boards (Fig. 5a) on all sides to exclude the possibility of convective heat loss through the insulation gaps. A chamfered square hole the size of the aperture area of the receiver (0.25 m × 0.25 m) was cut into the bottom insulation (with a maximum chamfer width of 0.4 m), as shown in Fig. 5b. A ceramic fibre blanket was placed externally between each coil and in the remaining air spaces (Fig. 6) to reduce the heat transfer area and to reduce the possibility of convective heat loss through the insulation gaps to the environment. Thermocouples were placed on the outside of the insulation layers, in-line with the weld-on thermocouples to obtain a temperature gradient through the insulation for conduction heat loss calculations.

2.4. Process air supply

Air was supplied to the system using a Husqvarna 580BTS two-stroke

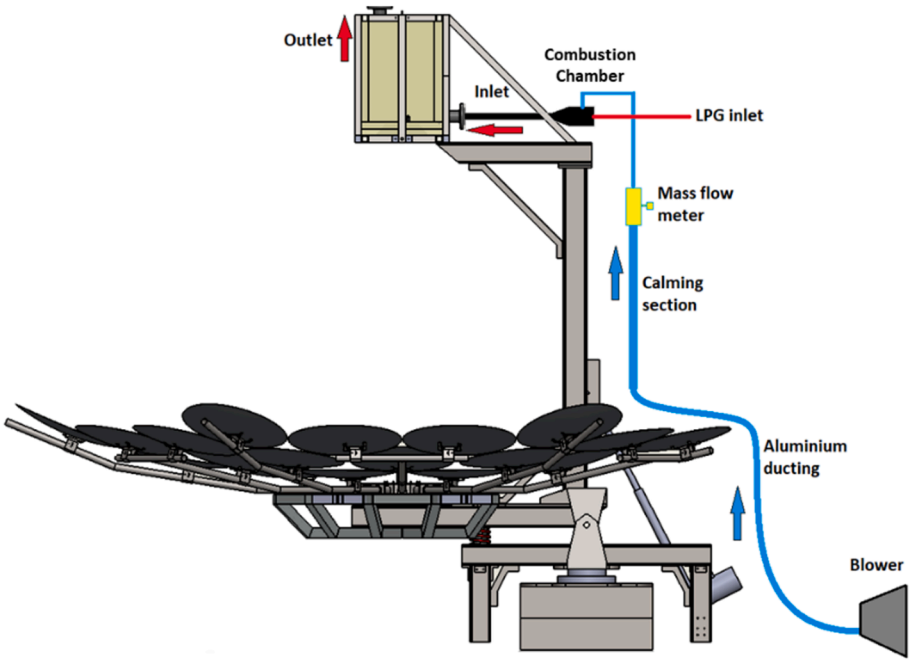

Fig. 1. Experimental test setup.

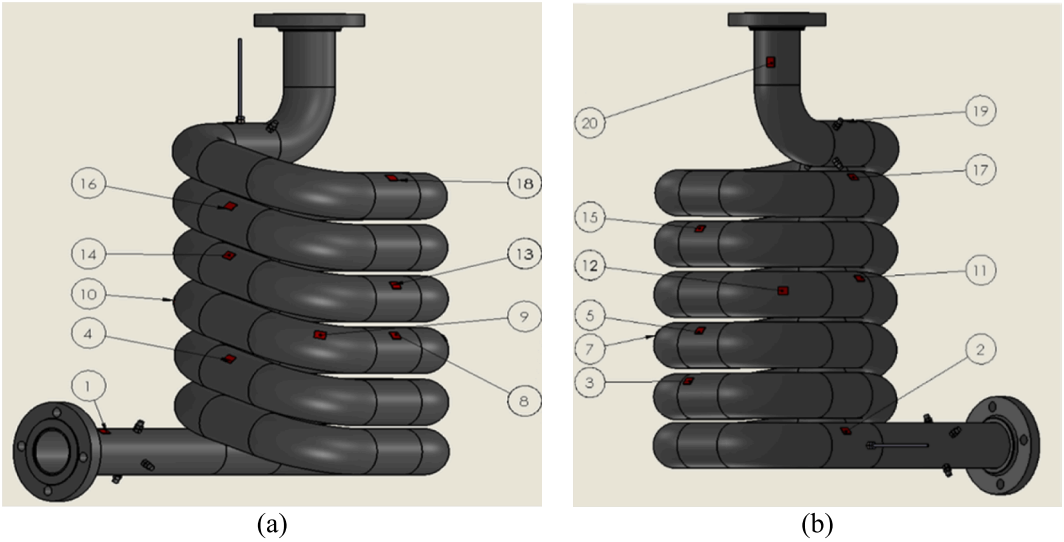

Fig. 2. Weld-on thermocouple arrangement along receiver pipe (a) front and right side, and (b) back and left side.

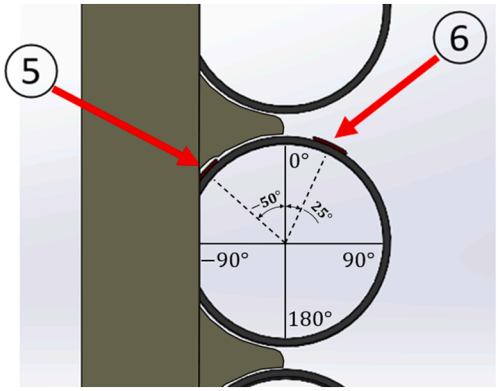

Fig. 3. Cross-section of coil turn three with positions of surface thermocouple 5 (outer cavity / insulation side) and surface thermocouple 6 (inner cavity).

backpack leaf blower. This leaf blower model was found to provide sufficient airflow to overcome the pressure loss through the system and provide the desired air mass flow rates. The air mass flow rate was measured by a SUTO S421 thermal mass flow sensor before the air entered the combustion chamber. An 80-mm-diameter and 2-m-length PVC pipe was used for the calming section before entering the mass flow meter to ensure accurate measurements [19]. The blower was connected to the calming section with 2.5 m long flexible aluminium ducting. The entire experimental setup is shown in Fig. 7.

2.5. Gas system

LPG was provided by four 48-kg gas bottles with two bottles connected in series and then in parallel with a similar branch using an LPG manifold system. An Afrox Saffire S6000 LGS 400 Single-Stage LPG regulator with a gauge was used to control the pressure at which LPG was provided to the combustion chamber. A Sievert valve was used after the regulator to control the gas flow rate into the combustion chamber.

2.6. Combustion chamber

The combustion chamber connected to the inlet of the receiver was wrapped with a ceramic fibre blanket to ensure effective heat transfer to the process air and to prevent sensor cables under the aluminium cover from melting. Two 90-degree elbows were used to connect the combustion chamber to the receiver to prevent the inlet thermocouples from being exposed to radiation from the combustion flame as this could affect temperature readings.

2.7. Data accumulation

The wind speed and direction were measured using a NAVIS W110-4–20/WSD model wireless sensor. The wind sensor was able to measure wind speeds from 0 to 50 m/s with an accuracy of ±2.5% and a resolution of 0.1 m/s. The wind direction was measured using a wind vane therefore the measured direction defined the direction that the wind was coming from. The wind direction was measured in degrees from 0° to

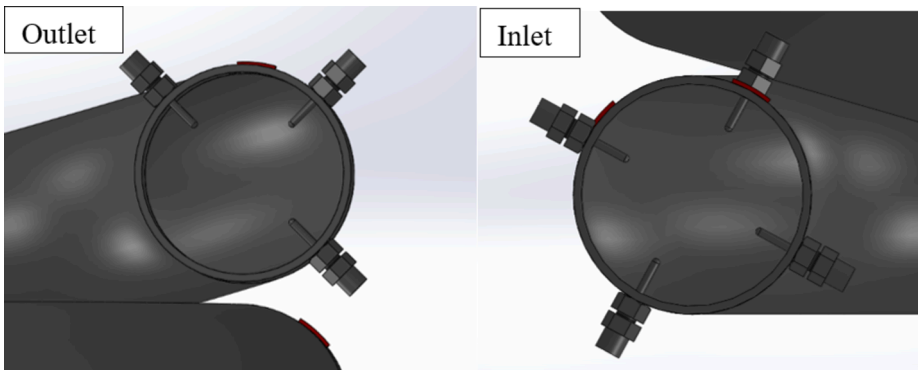

Fig. 4. Insert thermocouple arrangement.

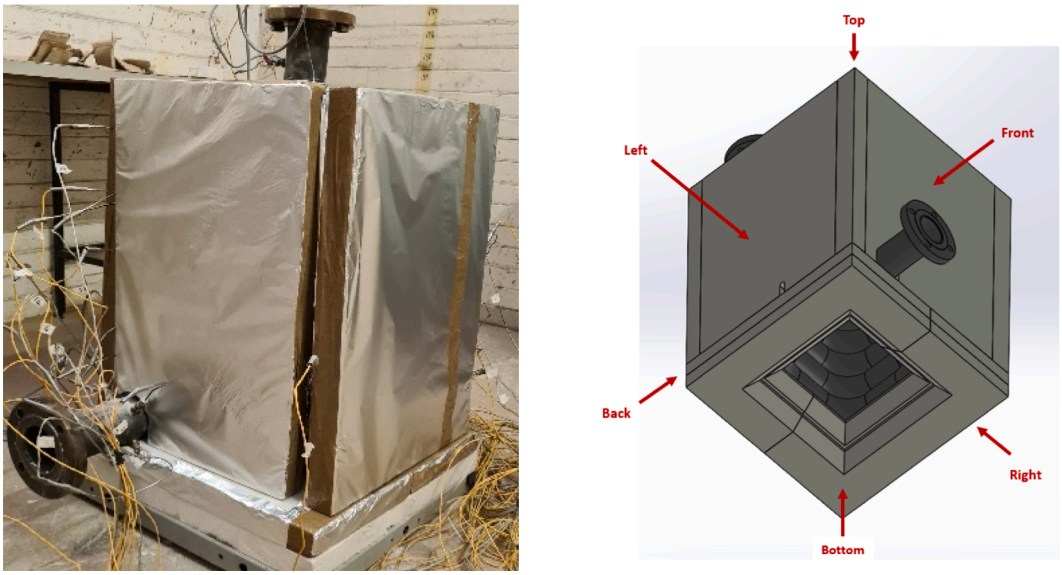

Fig. 5. Receiver coil with insulation showing (a) experimental model with aluminium foil covering and (b) CAD model with square aperture shown.

Fig. 6. Receiver with ceramic fibre blanket between coils.

360° with a resolution of 1° and accuracy of ±2.5° [20]. All temperature, flow and wind data were recorded by a Keysight 34972A LXI data acquisition unit and sent to a laptop through a USB cable. The SUTO mass flow sensor required a power supply of 15–30 VDC and 2 mA. This was supplied by a QJE PS3020 power supply. An aluminium cover (Fig. 7) was placed over the whole receiver and combustion chamber during outdoor testing to protect the insulation and sensors from the weather.

3. Testing methodology

Testing was conducted from May 2021 to October 2021. The data accumulation system was run to measure the initial conditions of the receiver before disturbance to the system as well as to check that all the sensors were calibrated correctly and providing measurement readings. Temperature, pressure, wind speed and wind direction measurements were recorded every 3 s. The blower was started and set to idle to provide sufficient air needed for combustion ignition. The LPG regulator was set to a pressure of 380 kPa. The spark plug in the combustion chamber was activated and the Sievert LPG valve was slowly opened until ignition was achieved in the combustion chamber. After ignition, the spark plug was switched off and the receiver inlet temperature was controlled using the LPG flow rate (using the Sievert valve). The inlet temperature was initially set to above 800 °C to speed up heating the coils to the desired temperature. The air mass flow rate (controlled with the blower throttle) and LPG flow rate were continuously adjusted to keep the system at the desired receiver inlet temperature and air mass flow rate. Air and gas flow rates were kept constant until steady state was reached. Steady state was defined as the state at which all

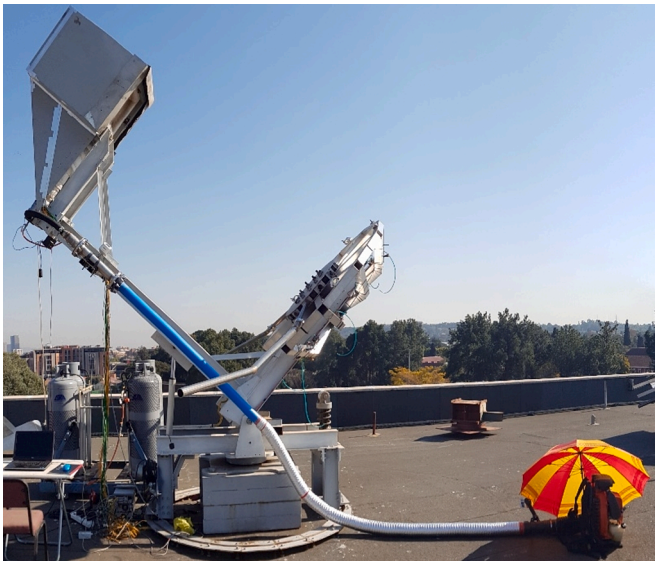

Fig. 7. Husqvarna blower connected to the calming section, mass flow meter and combustion chamber mounted on the test rig.

temperature readings were constant. The system was left to run at steady state for at least 5 min to have enough data available for analysis.

The inlet temperature was kept within ±5 °C of the desired receiver inlet temperature as it proved to be difficult to obtain a constant inlet temperature because the air and LPG mass flow rates were controlled manually for the combustion process. The elevation angle was defined as the angle above the horizon that the receiver was positioned (see Fig. 8a). The elevation angles at which the receiver was assessed are shown in Fig. 8b. The tracker's azimuth angle remained stationary throughout testing at 212°. Inlet temperatures were parameterised from 450 °C, 500 °C, 550 °C and 650 °C and mass flow rates varied between 0.03 kg/s to 0.07 kg/s.

3.1. Total heat loss

As heated air and combustion products passed through the receiver pipe, heat from the air was transferred to the environment through the cavity and insulation walls. The temperature of the air decreased along the length of the receiver pipe. With the temperature of the air and combustion products measured at the receiver inlet and outlet, the total heat loss rate from the gas mixture was calculated at steady state using Equation (1). The calculation was performed assuming that the combusted gas mixture had the same properties as air since combustion outlet temperatures were well below the adiabatic flame temperature, therefore, combustion in excess air was assumed. All air properties used in calculations were obtained using the CoolProp [21] add-in in Excel.

$$\dot{Q}_{tot} = \dot{m}(h_{in} - h_{out}) \tag{1}$$

In the case of internal flow through a pipe at high temperature, the instream thermocouples at the inlet and outlet of the receiver were not only exposed to the working fluid temperature (convection) but also to the temperature of the surrounding pipe cavity (radiation). Çengel and Ghajar [22] propose a method to account for the radiation effect using Equation (2).

$$T_f = T_{th} + \frac{\varepsilon\sigma\left(T_{th}^4 - T_{wall}^4\right)}{\widehat{h}} \tag{2}$$

The emissivity of the thermocouple is assumed to be the same as the receiver coil with a normal total emittance range of 0.69 to 0.74 for thermocouple temperatures of between 386 K and 1303 K [23]. The convective heat transfer coefficient was calculated from the average Nusselt number for cross flow over a cylinder. Churchill and Bernstein [24] proposed such a relationship (see Equation (3)) that was valid for $RePr > 0.2$, which was within the application range of the current study. The measurements of surface thermocouples 1 and 19 were used as T_{wall} for the inlet and outlet air temperature measurements as they were placed at the same location along the length of the receiver as the inlet and outlet in-stream thermocouples (see Fig. 2).

$$Nu = \frac{\widehat{h}D_{th}}{k} = 0.3 + \frac{0.62Re^{\frac{1}{2}}Pr^{\frac{1}{3}}}{\left(1 + \left(\frac{0.4}{Pr}\right)^{\frac{2}{3}}\right)^{\frac{1}{4}}}\left[1 + \left(\frac{Re}{282000}\right)^{\frac{5}{8}}\right]^{\frac{4}{5}} \tag{3}$$

The pressure at the outlet of the receiver was assumed to be ambient pressure since the outlet was open to the ambient. The inlet pressure to the receiver was estimated as function of ambient pressure and mass flow rate according to Equation (4) and Equation (5). The ΔP_{rec} term was experimentally established through separate ambient temperature pressure drop tests where the pressure coefficient (C_p) is modelled with a coefficient $\overline{A}$ which is 7.47E5 and a coefficient $\overline{B}$ which is −1.12. The Reynolds number for Equation (5) was determined at bulk fluid temperature through the coil pipe with the coil pipe inner diameter used as the characteristic length.

$$P_{in} = P_{amb} + \Delta P_{rec} \tag{4}$$

$$\Delta P_{rec} = \frac{1}{2}\rho V^2 \times C_p = \frac{1}{2}\rho V^2 \times \overline{A}Re^{\overline{B}} \tag{5}$$

3.2. Conductive heat loss

For the case of a rectangular receiver, the method of conduction heat loss through a plane wall was used for the sides, bottom, and top of the receiver. Inner-cavity cross-sectional areas were used in the conduction heat loss calculation. Conduction through the corners of the side walls was assumed negligible based on previous studies [16,25]. Conduction through a planar wall with insulation thickness (L) was calculated using Equation (6).

$$\dot{Q}_{cond} = \sum \frac{k_i A_{wall_i}\left(T_{wall_i} - T_{ins_i}\right)}{L} \tag{6}$$

The conduction heat loss through each wall (front, back, right, left, top and bottom – see Fig. 5b) was calculated separately and added together to obtain the total conduction heat loss of the receiver. The ceramic fibre material has a thermal conductivity ranging from 0.067 W/mK to 0.136

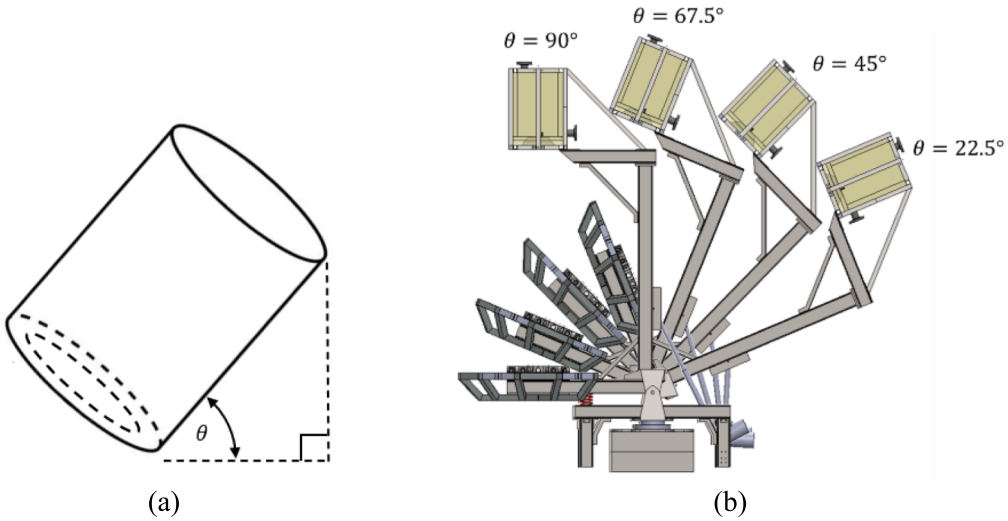

Fig. 8. (a) Elevation angle of the receiver cavity, (b) Receiver elevation angles for the testing period.

W/mK for temperatures ranging from 400 °C to 800 °C [18]. The thermal conductivity was calculated as a function of the average insulation temperature between the inner and outer wall surfaces.

4. Analytical model

Radiation heat loss and convection heat loss were analytically determined by considering the internal geometry of the receiver cavity (see Fig. 9). The receiver cavity had a side length of $a_{cav} = 0.25m$, and a cavity height of $h_{cav} = 0.678m$. The aperture length (distance between aperture sides) was the same as the side length of the cavity (distance between inner cavity sides/coils). The interior geometric surface area (planar area) of the cavity ($A_{cav,p} = 0.741m^2$) was determined by approximating the inner-cavity sides as being a rectangular prism with dimensions equivalent to the product of the cavity side length and cavity height as shown in Equation (7).

The interior geometric surface area of the heat transfer tubing ($A_{tube,p} = 0.505m^2$, see Equation (8)) was determined by projecting tube length and diameter onto the simplified rectangular prism ($L_{tube,p} = 5.68m$, and $D_{tube,o} = 88.9mm$). The exposed tube surface area within the cavity was determined using Equation (9), by estimating the centreline length of the coil (L_{tube}). The heat transfer surface areas negate the wind skirt when working with cavity area since the wind skirt is not heated and is close to ambient temperature.

$$A_{cav,p} = 4h_{cav}a_{cav} + a_{cav}^2 \tag{7}$$

$$A_{tube,p} = L_{tube,p} \times D_{tube,o} \tag{8}$$

$$A_{tube} = L_{tube} \times \frac{\pi D_{tube,o}}{2} \tag{9}$$

4.1. Radiative heat loss

The radiative heat loss from the receiver aperture was calculated using the direct radiosity method as presented in Equation (10) and Equation (11) [22], which was also implemented by Abbasi-Shavazi et al. [26] and McDonald [27]. Gray and opaque surfaces were assumed. The inner cavity was simplified to a 0.25 m × 0.25 m × 0.678 m rectangular prism in a comparable manner to Equation (7). The rectangular prism was discretized to demarcate the aperture, the seven coil turns and the top of the receiver cavity. Each of the seven coil turns were discretized equally at a 0.097 m height. The top of the receiver inside the cavity comprised of ceramic fibre blanket and was assumed to have the same temperature as the average temperature of the coil surfaces inside the cavity. The emissivity of each coil turn was determined as a function of wall temperature for stainless steel stably oxidized at 1255 K [23]. Normal total emittance values were the same as was used in Equation (2). For radiation calculations, the average temperature of the thermocouples placed on the surface of the receiver coil within the cavity was used. The ambient temperature, T_{amb}, used in calculations was the average ambient temperature measured by the SAURAN station at the University of Pretoria for the testing time interval [28].

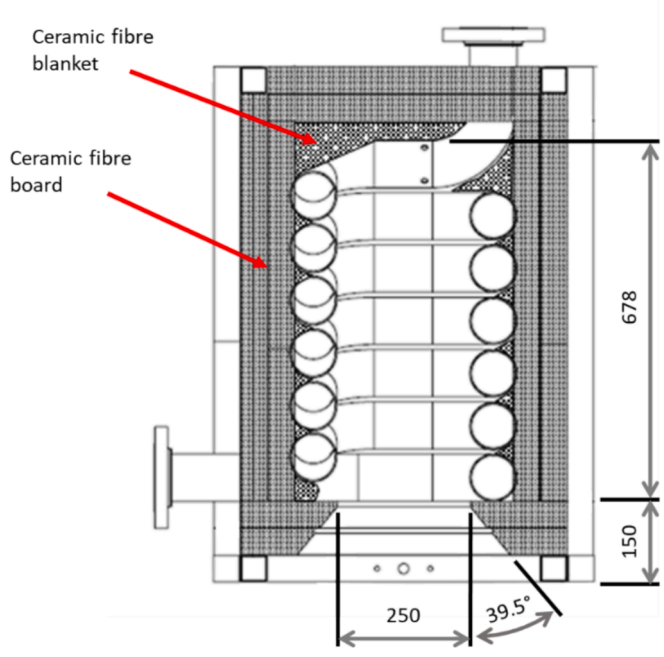

Fig. 9. Illustration of primary receiver cavity dimensions (lengths in mm) used in analytical model.

$$\sigma T_i^4 = J_i + \frac{1-\varepsilon_i}{\varepsilon_i} \sum_{j=1}^{N} F_{i-j}\left(J_i - J_j\right) \tag{10}$$

$$\dot{Q}_{rad} = A_{ap} \sum_{j=1}^{N} F_{ap-j}\left(J_{ap} - J_j\right) \tag{11}$$

4.2. Convective heat loss

As there were three heat loss mechanisms present (radiation, conduction, and convection) during steady-state, the convection heat loss rate from the receiver can be expressed by Equation (12).

$$\dot{Q}_{conv} = \dot{Q}_{tot} - \dot{Q}_{cond} - \dot{Q}_{rad} \tag{12}$$

4.3. Natural convection

Multiple correlations have been proposed in literature to model natural convection heat loss from cylindrical cavity receivers [1]. The few correlations chosen for the current study were regarded as being more popular or were found to be valid within the current operating range. The current receiver under investigation was rectangular with a square aperture. To approximate a cylindrical cavity, Equation (13) determines an equivalent aperture diameter of 0.28 m that equates to the current aperture area. Both aperture and cavity diameters used in the following correlations were determined this way ($D_{ap} = D_{cav}$).

$$A_{ap} = a_{ap}^2 = \frac{\pi}{4} D_{ap}^2 \tag{13}$$

Koenig and Marvin [29], presented by Harris and Lenz [4], developed a correlation (see Equation (14) and Equation (15)) for natural convection heat loss from a high temperature cylindrical cavity receiver with cavity temperatures of between 550 °C and 900 °C. The heat loss due to natural convection was determined using Equation (15). The area used for the correlation was the exposed surface area of the tubing inside the cavity.

$$Nu_{nat} = \frac{\widehat{h}_{nat} L_c}{k} = 0.52p(\theta)\tau^{1.75}(Gr_{L_c}Pr)^{\frac{1}{4}} \tag{14}$$

$$\dot{Q}_{conv,nat} = \widehat{h}_{nat} A_{tube}\left(T_{cav,inner} - T_{amb}\right) \tag{15}$$

Stine and McDonald [30] suggested an improved correlation in 1988 (Equation (16) and Equation (17)) for calculating the Nusselt number for natural convection heat loss by modifying the equation used in the Koenig and Marvin method by changing the constant, 0.52, to 0.78 and using the interior geometric surface area $(A_{cav,p})$ in heat loss calculations. The characteristic length (L_c) was kept the same as that of Koenig and Marvin [29].

$$Nu_{nat} = \frac{\widehat{h}_{nat} L_c}{k} = 0.78\mathrm{p}(\theta)\tau^{1.75}(Gr_{L_c}Pr)^{\frac{1}{4}} \tag{16}$$

$$\dot{Q}_{conv,nat} = \widehat{h}_{nat} A_{cav,p} \left(T_{cav,inner} - T_{amb}\right) \tag{17}$$

A second correlation (Equation (18) to Equation (20)) was developed by Stine and McDonald [31] in 1989, presented by McDonald [27], to calculate the natural convection Nusselt number for a cylindrical open-cavity receiver with different aperture lengths. This second correlation was a modification of the Siebers and Kraabel model which considered the effects of different receiver temperatures, elevation angles and aperture sizes and correlated well with experimental results [32]. The model of Siebers and Kraabel [32] overestimated the natural convection heat loss in comparison to the experimental results in McDonald [27]. The area used for the correlation was the interior geometric surface area of the tubing inside the cavity ($A_{tube,p}$). The characteristic length (L_c) was defined as the cavity inner diameter.

$$Nu_{nat} = \frac{\widehat{h}_{nat} L_c}{k} = 0.088 Gr_{L_c}^{\frac{1}{3}} \left(\frac{T_{cav,inner}}{T_{\text{amb}}}\right)^{0.18} (cos\theta)^{2.47} \left(\frac{D_{ap}}{L_c}\right)^{s} \tag{18}$$

$$s = 1.12 - 0.98\left(\frac{D_{ap}}{L_c}\right) \tag{19}$$

$$\dot{Q}_{conv,nat} = \widehat{h}_{nat} A_{tube,p} \left(T_{cav,inner} - T_{amb}\right) \tag{20}$$

The correlation of Wu et al. [33] (Equation (21) and Equation (22)) defined natural convection heat loss as a function of cavity surface temperature, elevation angle, aperture length to cavity ratio and aperture position. The characteristic length (L_{cav}) was defined as the inner-cavity diameter. AP was defined as the dimensionless aperture position and for centrally located apertures, $AP = 0.5$. The area used for the correlation was the total inner-cavity surface area based on a planar cavity numerical model. In the current study, the planar cavity surface area ($A_{cav,p}$) was assumed which includes exposed tubing as well as exposed insulation surface. Equation (17) was used to calculate the natural convection heat loss from the receiver cavity.

$$Nu_{nat} = \frac{\widehat{h}_{nat} L_c}{k} = 1.87845 \times 10^{-3} Gr_{L_c}^{\frac{1}{3}} \left(\frac{T_{cav}}{T_{amb}}\right)^{0.709}$$

$$\times (1 + cos\theta)^{4.7802} \tau^{1.9752} AP^{0.2749} \tag{21}$$

$$\tau = \frac{D_{ap}}{D_{cav}} \tag{22}$$

Abbasi-Shavazi et al. [26] developed a correlation in 2020 (Equation (23) to Equation (25)) that considered the temperature distribution within the cavity using the temperature coefficient T^*. T_{max} and T_{min} are the respective maximum and minimum surface temperatures in the cavity. The correlation also considered the air flow dynamics within the cavity receiver by considering the convection zone and stagnation. The characteristic length was determined by taking the elevation angle into account through $D_{ap\perp}$ which is the vertical projection of the aperture diameter (see Equation (26)). AR is the aspect ratio of the cavity (cavity length divided by the aperture length). The cavity length includes the additional 0.15 m height of the aperture wind skirt to the cavity height (see Fig. 9).

$$Nu_{nat} = \frac{\widehat{h} L_c}{k} = 0.126 (Gr_{L_c})^{\frac{1}{3}} (T^*)^{0.11} AR^{-0.52} \left(\frac{A_{cav,cz}}{A_{cav,p}}\right)^{0.80} \tag{23}$$

$$L_c = D_{ap\perp} + \frac{D_{ap}}{2} \tag{24}$$

$$T^* = \frac{T_{max} - T_{\text{amb}}}{T_{min} - T_{\text{amb}}} \tag{25}$$

The exposed cavity wall surface used in Equation (27) from Abbasi-Shavazi et al. [26] was defined as the total exposed surface area within the cavity for a planar cavity model. Equation (17) was used to calculate the natural convection heat loss from the receiver cavity. The convective zone surface area ($A_{cav,cz}$) was determined by considering Equation (27) and Equation (28).

$$D_{ap\perp} = D_{ap} \cos(\theta) \tag{26}$$

$$A_{cav,cz} = A_{ap} + A_{cz} \tag{27}$$

$$A_{cz} = \frac{2a_{cav}^2}{tan(\theta)} \tag{28}$$

It is important to note that the Abbasi-Shavazi et al. [26] model accounts for nonuniform cavity temperature during on-sun conditions through the T^* term. Due to the nature of heating during on-sun conditions the T^* term was developed for values greater than one with the max coil temperature occurring at the back of the cavity relative to the aperture. Since the process air running through the receiver coil was cooled down by the ambient in the current study, the maximum coil surface temperature occurred near the inlet of the receiver (see Fig. 11). For this reason, a uniform cavity temperature was assumed with $T^* = 1$.

4.4. Forced convection

Ma [34] conducted experiments on an open cavity receiver to determine the effects of forced convection due to side-on and head-on winds towards the cavity aperture at a cavity temperature of 550 K and an ambient temperature of 294 K. The receiver of Ma [34] had a full interior surface area of 1.472 m^2 which was comparable to that of the current study which was 1.476 m^2 [16]. There was also similarity in the design of the receiver aperture where a wind skirt or wind break was incorporated, resulting in the receiver coil being located deeper within the receiver cavity [27,34]. Side-on winds are defined by traveling parallel to the ground and incident of the right and left sides of the receiver (parallel to the aperture plane – see Fig. 5b). Head-on winds are defined as travelling parallel to the ground and being incident on the 'front' of the receiver (incident on the 'bottom'/aperture at elevation angles below 90°). Back-on winds were not studied by Ma [34], but are defined as traveling parallel to the ground and being incident on the 'back' of the receiver (incident on the 'back' and 'top' of the receiver at elevation angles below 90°).

According to the results obtained by Ma [34], the correlation for the forced convection heat transfer coefficient for side-on winds is given in Equation (29) and the correlation for the forced convection heat transfer coefficient for head-on winds is given in Equation (30) and Equation (31). The convective area used was the full interior geometric surface area of the cavity ($A_{cav,p}$). It should be noted that Equation (29) and Equation (30) are based on the specific receiver that was tested by Ma [34] with only a few data points, thus it is not necessarily applicable to all cavity receivers.

$$\widehat{h}_{forced,side} = 0.1967 V_{side}^{1.849} \tag{29}$$

For head-on winds:

$$\widehat{h}_{forced,head} = f(\theta) V_{head}^{1.401} \tag{30}$$

$$f(\theta) = 0.1634 + 0.7498\sin(\theta) - 0.5026\sin(2\theta) + 0.3278\sin(3\theta) \tag{31}$$

For wind incident angles between pure side-on and pure head-on conditions, the respective wind vectors were determined, and the resulting heat transfer coefficients were combined using root sum of squares as presented in Equation (32). Back-on wind components were assumed negligible and were not included in the forced convection heat loss calculation (except for the receiver positioned at a 90° elevation angle where all wind directions were considered side-on wind components).

$$\widehat{h}_{forced} = \sqrt{\widehat{h}^2_{forced,side} + \widehat{h}^2_{forced,head}} \quad (32)$$

The natural and forced components were assumed additive according to Ma [34]. To obtain the combined free-forced convection heat loss, the natural convection heat loss determined by the correlations in Section 4.2.1 and the forced convection heat loss of Ma [34] were added according to Equation (33).

$$\dot{Q}_{conv} = \dot{Q}_{conv,forced} + \dot{Q}_{conv,nat} \quad (33)$$

5. Results and discussion

For illustration purposes, sample test data from a specific day of testing are presented in Section 5.1 and the time-dependent test results are discussed along with a steady-state cavity temperature sample. Steady-state periods over 5-minute intervals were defined using the conditions in Table 1. Wind speeds varied between 0.5 m/s and 3 m/s, on average, during testing. A summary of the total heat loss rates and convection heat loss rates are discussed in Section 5.2 and Section 5.3, respectively.

5.1. Sample data

Fig. 10 presents test sample data from the 19th of July 2021. The plot shows the corrected inlet and outlet process air temperatures, inlet and outlet pipe wall temperatures and average outer coil surface temperature (outer-cavity temperature) measurements for a receiver elevation angle of 90° and a target inlet temperature of 450 °C (723 K). The corrected inlet and outlet process air temperatures will be referred to as inlet and outlet temperatures for the rest of the article. The percentage correction in Kelvin for the inlet air temperature ranged between 0.2 % and 0.9 % while the percentage correction for the outlet air temperature ranged between 0.4 % and 1.7 % for all parameterised steady-state data points captured (for the radiation effect on thermocouples).

Initial heating of the receiver coil is shown in Fig. 10 with an elevated inlet air temperature. The inlet air temperature was then manually lowered and maintained at the target inlet air temperature until the cavity temperature reached a steady state. An inlet temperature fluctuation is visible in Fig. 10 however the outlet temperature and average coil surface temperature measurements appear stable. It was important to ensure that the inlet conditions (inlet air temperature and air mass flow rate) were stable, and this was done by manually adjusting the air blower speed setting and the fuel supply into the combustion chamber. Wind speed and direction fluctuated erratically throughout testing (see wind data in Appendix B) which represented naturalistic field operations more accurately. The wind direction given in Tables 3 to 6 were averages but the wind directions deviated from the average by up to 160° during the 5-minute steady-state data points. As a result, there is an inherent fluctuation of the resulting total heat loss and convection heat loss at parameterised cavity temperatures (as will be shown in Tables 3 to 6).

During parametric testing, the duration towards steady-state of the outer insulation temperature was impractically long as it heated up from the air being passed through the receiver coil. A simplifying approximation assumed steady state of the outer insulation temperature when the heat loss and cavity temperature steady-state conditions were met (see Table 1). The ranges in outer insulation temperature measurements (per side – see Fig. 5b) for the given steady-state period were averaged to form the approximated steady-state outer insulation temperatures and were used in the conduction heat loss calculations.

Table 1
Steady-state conditions over a 5-minute period.

Description	Value	Units
Total heat loss standard deviation	<150	W
Cavity temperature slope	±0.01	K/minute

Fig. 11 shows the steady-state coil surface thermocouples' readings along the length of the coil for a receiver elevation angle of 90° and a target inlet temperature of 450 °C. The corrected inlet temperature (shown in Fig. 11) turned out to be 4 °C higher than the target inlet temperature due to the radiation effect and subsequent correction. The surface thermocouples were distributed throughout the length of the receiver coil with surface thermocouple number 1 placed at the inlet of the receiver and number 20 at the outlet of the receiver (see Fig. 2). The surface thermocouple readings decrease along the length of the coil as shown in Fig. 11. A notable decrease was observed from thermocouple 1 to thermocouple 3 and from thermocouple 19 to thermocouple 20. This was due to the areas of the receiver coil being located outside the cavity and inadequately insulated. This however does not affect the results as the average outer-cavity temperature was determined from surface thermocouples located inside the insulated receiver cavity. Surface thermocouples 3–5, 7, 9–11, 13, 14 and 16–19 were used to calculate the average outer-cavity temperature (on the insulation side of the receiver coil). Surface thermocouple 2, 8, 12 and 15 were not used to calculate the average outer-cavity temperature and are not shown in Fig. 11 as they proved to be faulty during testing. The outer-cavity surface temperature of coil turn 1 (where surface thermocouple 2 was located) was estimated to be the same temperature as the outer-cavity surface temperature of coil turn 2. This assumption was based on test results during instances when surface thermocouple 2 was operating, which showed a temperature difference of less than 1 % in Kelvin.

Surface thermocouple 6 in Fig. 11 was exposed to the inner cavity at the same coil as surface thermocouple 5 (see Fig. 3). Radiation and convection heat losses are functions of the discretized inner-cavity temperature per coil turn and the average inner-cavity temperature, respectively. Therefore, the inner-cavity temperature per coil turn was estimated from the CFD results of Craig et al. [16]. Coil surface temperature contours for each coil turn were produced in the study of Craig et al. [16] for a validation case study at 90° elevation, no-sun condition and 3 m/s windspeed. The average cross-sectional surface temperature for each coil turn was normalized against their respective maximum temperatures in Kelvin (see Fig. 12). 0° refers to the top and ±180° refers to the bottom of the respective pipe cross-section (see insert in Fig. 12). The negative angular range, in Fig. 12, refers to the outer cross section of pipe in contact with the cavity insulation and the positive range refers to the cross section of pipe exposed to the inner cavity. Conversion factors for each coil turn (see Table 2) were determined from the ratio between the average normalized temperature of the coil surface exposed to the inner cavity (between 45° and 135°) and the normalized temperature at the estimated location of the outer-cavity surface thermocouples (−50°, see Fig. 12).

The average inner-cavity temperature ($T_{cav,inner}$) was determined from the inner-cavity surface temperatures of the coil (average inner-cavity surface temperature of the 6.5 coils) as well as the insulation exposed to the inner cavity (see Appendix B). The ratio of the average inner-cavity temperature ($T_{cav,inner}$ – determined using the conversion factors) to the measured average outer-cavity temperature ($T_{cav,outer}$) was comparable to the temperature ratio of surface thermocouple 6 (located at 25° in Fig. 3 and Fig. 12) to surface thermocouple 5 (located at −50° in Fig. 12) which ranged between 0.98 and 0.99 (see Appendix B), supporting the use of the conversion factors in Table 2.

5.2. Total heat loss

The total heat loss rate from the receiver was determined using Equation (1) for the steady-state points of interest (see Tables 3 to 6, and Appendix B). It was observed that the total heat loss rates between the 45° elevation angle and the 67.5° elevation angle (as a function of cavity temperature) are effectively equal. Overall, total heat loss rates (as a function of cavity temperature) at elevation angles of 67.5°, 45° and

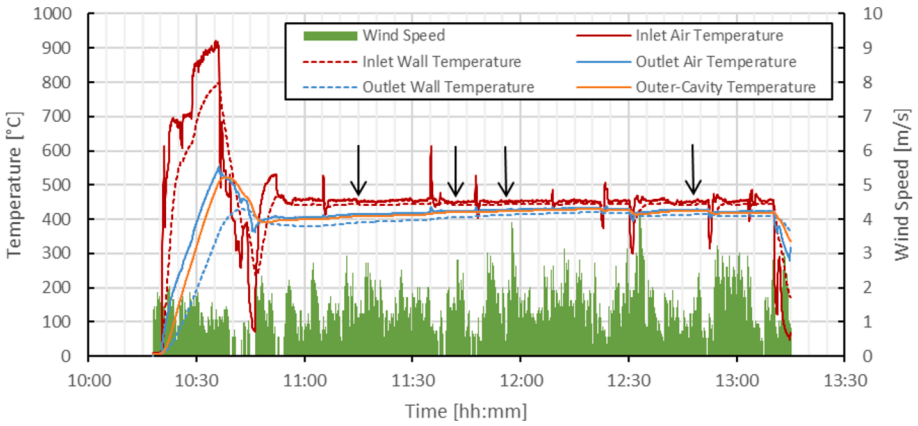

Fig. 10. Receiver temperature measurements for 450 °C target inlet temperature, at 90° receiver elevation angle (Date: 19/07/2021). The black arrows indicate the steady-state points of interest identified.

Table 2
Conversion factors from CFD results of Craig et al. [16]. Used to determine average surface temperatures of the coil turns exposed to the inner cavity (in Kelvin) from the coil surface temperature measurements located on the outer cavity.

Description	Conversion factor
Coil 1	0.962
Coil 2	0.971
Coil 3	0.984
Coil 4	0.991
Coil 5	0.994
Coil 6	0.996
Coil 6.5	0.996

22.5° increased by 16 %, 9 % and 61 % respectively when compared to the total heat loss rate at 90°.

5.3. Convection heat loss

The experimental free-forced convection heat loss data points were determined from Equation (12) and are presented along with total heat loss, conduction heat loss and radiation heat loss in Tables 3 to 6. The free-forced convection heat loss for the respective natural convection heat loss correlations in literature (see Section 4.2.1) were determined according to Section 4.2.2 and compared with the experimental convection heat loss according to Equation (34).

$$\Delta\dot{Q}_{conv} = \frac{\dot{Q}_{conv,cor} - \dot{Q}_{conv,Eq1}}{\dot{Q}_{conv,Eq1}} \tag{34}$$

Table 3
Averaged 90° elevation angle cavity heat loss values (in Watts) for steady-state data points. Natural convection heat loss correlations from literature are superimposed with forced convection heat loss of Ma [34].

Sample	$\dot{Q}_{tot}$	$\dot{Q}_{cond}$	$\dot{Q}_{rad}$	$\dot{Q}_{conv}$ (Eq. (1))	$\Delta\dot{Q}_{conv}$ [29]	$\Delta\dot{Q}_{conv}$ [30]	$\Delta\dot{Q}_{conv}$ [31]	$\Delta\dot{Q}_{conv}$ [33]	$\Delta\dot{Q}_{conv}$ [26]
1	1237	370	201	666	−34 %	−34 %	−34 %	−8%	58 %
2	1274	360	240	674	−71 %	−71 %	−71 %	−48 %	7 %
3	1357	364	363	630	−67 %	−67 %	−67 %	−53 %	−17 %
4	1597	371	549	677	−67 %	−67 %	−67 %	−57 %	−32 %
5	1769	430	256	1083	−30 %	−30 %	−30 %	−3%	58 %
6	1827	401	561	865	−56 %	−56 %	−56 %	−45 %	−20 %
7	1889	450	309	1130	−40 %	−40 %	−40 %	−17 %	34 %
8	1919	430	374	1115	10 %	10 %	10 %	28 %	70 %
9	2004	448	486	1069	−68 %	−68 %	−68 %	−54 %	−22 %
10	2297	485	365	1446	85 %	85 %	85 %	108 %	154 %
11	2367	495	505	1366	−94 %	−94 %	−94 %	−78 %	−45 %
12	2594	492	767	1335	−59 %	−59 %	−59 %	−48 %	−27 %

The last five columns are respectively associated with the following authors: Koenig and Marvin [29], Stine and McDonald (1988) [30], Stine and McDonald (1989) [31], Wu et al. [33], Abbasi-Shavazi et al. [26].

Table 4
Averaged 67.5° elevation angle cavity heat loss values (in Watts) for steady-state data points. Natural convection heat loss correlations from literature are superimposed with forced convection heat loss of Ma [34].

Sample	$\dot{Q}_{tot}$	$\dot{Q}_{cond}$	$\dot{Q}_{rad}$	$\dot{Q}_{conv}$ (Eq. (1))	$\Delta\dot{Q}_{conv}$ [29]	$\Delta\dot{Q}_{conv}$ [30]	$\Delta\dot{Q}_{conv}$ [31]	$\Delta\dot{Q}_{conv}$ [33]	$\Delta\dot{Q}_{conv}$ [26]
1	1988	447	458	1083	−10 %	−4%	−23 %	0 %	7 %
2	2018	389	777	851	−36 %	−33 %	−44 %	−33 %	−27 %
3	2529	480	734	1314	−40 %	−37 %	−49 %	−34 %	−30 %
4	2590	480	816	1294	−36 %	−33 %	−44 %	−30 %	−27 %
5	2715	479	954	1282	−49 %	−47 %	−56 %	−44 %	−41 %

The last five columns are respectively associated with the following authors: Koenig and Marvin [29], Stine and McDonald (1988) [30], Stine and McDonald (1989) [31], Wu et al. [33], Abbasi-Shavazi et al. [26].

Table 5
Averaged 45° elevation angle cavity heat loss values (in Watts) for steady-state data points. Natural convection heat loss correlations from literature are superimposed with forced convection heat loss of Ma [34].

Sample	$\dot{Q}_{tot}$	$\dot{Q}_{cond}$	$\dot{Q}_{rad}$	$\dot{Q}_{conv}$(Eq. (1))	$\Delta\dot{Q}_{conv}$ [29]	$\Delta\dot{Q}_{conv}$ [30]	$\Delta\dot{Q}_{conv}$ [31]	$\Delta\dot{Q}_{conv}$ [33]	$\Delta\dot{Q}_{conv}$ [26]
1	1809	420	309	1081	308 %	337 %	278 %	235 %	119 %
2	2001	422	467	1112	201 %	221 %	181 %	152 %	76 %
3	2190	370	1037	783	38 %	45 %	26 %	15 %	−10 %
4	2234	422	712	1100	96 %	109 %	83 %	64 %	14 %
5	2240	421	729	1090	89 %	101 %	76 %	58 %	9 %
6	2381	422	819	1140	53 %	64 %	42 %	25 %	−20 %
7	2461	467	639	1355	141 %	156 %	131 %	107 %	40 %
8	2611	458	762	1390	82 %	95 %	74 %	54 %	−3%
9	2618	464	801	1352	119 %	131 %	110 %	92 %	38 %

The last five columns are respectively associated with the following authors: Koenig and Marvin [29], Stine and McDonald (1988) [30], Stine and McDonald (1989) [31], Wu et al. [33], Abbasi-Shavazi et al. [26].

Table 6
Averaged 22.5° elevation angle cavity heat loss values (in Watts) for steady-state data points. Natural convection heat loss correlations from literature are superimposed with forced convection heat loss of Ma [34].

Sample	$\dot{Q}_{tot}$	$\dot{Q}_{cond}$	$\dot{Q}_{rad}$	$\dot{Q}_{conv}$(Eq. (1))	$\Delta\dot{Q}_{conv}$ [29]	$\Delta\dot{Q}_{conv}$ [30]	$\Delta\dot{Q}_{conv}$ [31]	$\Delta\dot{Q}_{conv}$ [33]	$\Delta\dot{Q}_{conv}$ [26]
1	2212	375	1056	780	132 %	149 %	72 %	40 %	−7%
2	2375	382	1168	825	108 %	124 %	53 %	23 %	−21 %
3	2587	386	1372	829	103 %	117 %	56 %	31 %	−6%
4	2891	435	1427	1028	121 %	135 %	77 %	49 %	2 %
5	3066	426	1665	976	67 %	79 %	30 %	7 %	−31 %

The last five columns are respectively associated with the following authors: Koenig and Marvin [29], Stine and McDonald (1988) [30], Stine and McDonald (1989) [31], Wu et al. [33], Abbasi-Shavazi et al. [26].

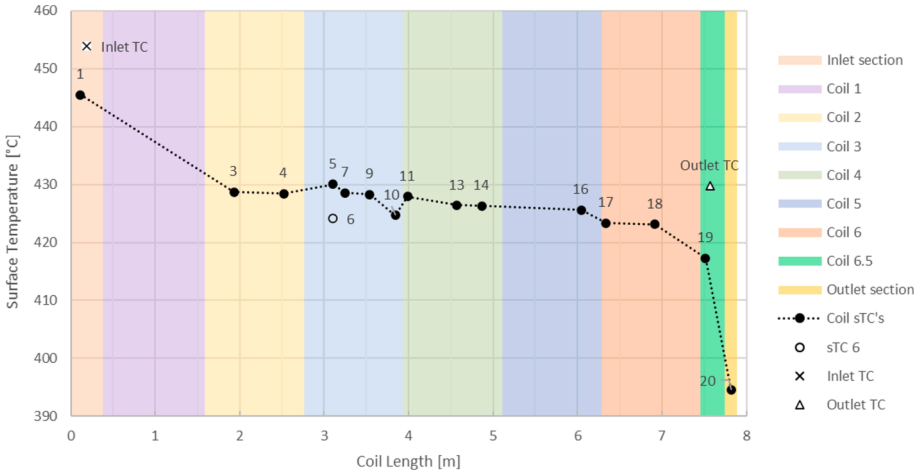

Fig. 11. An example of the steady-state coil surface thermocouple readings and corrected air temperature readings for a receiver elevation angle of 90°, constant mass flow rate of 50 g/s and a target inlet temperature of 450 °C (Time: 12:25–12:30, Date: 19/07/2021).

For a 90° elevation angle, it should be noted that the correlations of Koenig and Marvin [29], Stine and McDonald (1988) [30] and Stine and McDonald (1989) [31] estimate that no natural convection heat loss occurs and only the forced convection heat loss component from Ma [34] was present. The correlation of Abbasi-Shavazi et al. [26] was determined to model the experimental free-forced convection heat loss the closest with an average percentage difference of +3 % for elevation angles ranging between 22.5° and 90°, followed by Wu et al. [33] with an average percentage difference of +17 % (see Fig. 13). The correlation of Abbasi-Shavazi et al. [26] provided the best correlation due to its unique ability to model non-uniform inner-cavity surface temperature which allowed the current study to model the receiver coil deeper into the receiver cavity and account for the wind skirt. The successful, broad application of the correlation of Abbasi-Shavazi et al. [26] in multiple cavity geometries and datasets during the correlation's development also supports its current success.

Based on the analysis, it may be concluded that the experimental convection heat loss of an open-cavity tubular receiver (with a relatively large pipe diameter and a wind skirt) was shown to be within range of the convection heat loss estimated by the correlations of Abbasi-Shavazi et al. [26] and Wu et al. [33] superimposed with the forced convection of Ma [34]. It is therefore recommended that the natural convection correlations of Abbasi-Shavazi et al. [26] superimposed with the forced convection correlations of Ma [34] can be used to model convection heat loss from an open-cavity tubular receiver for a solar Brayton cycle with a relatively large pipe diameter and a wind skirt – specifically at average air mass flow rates of between 33 g/s and 68 g/s and at average inner-cavity temperatures of up to 550 °C.

6. Conclusion

Experimental heat loss analysis was conducted on a rectangular

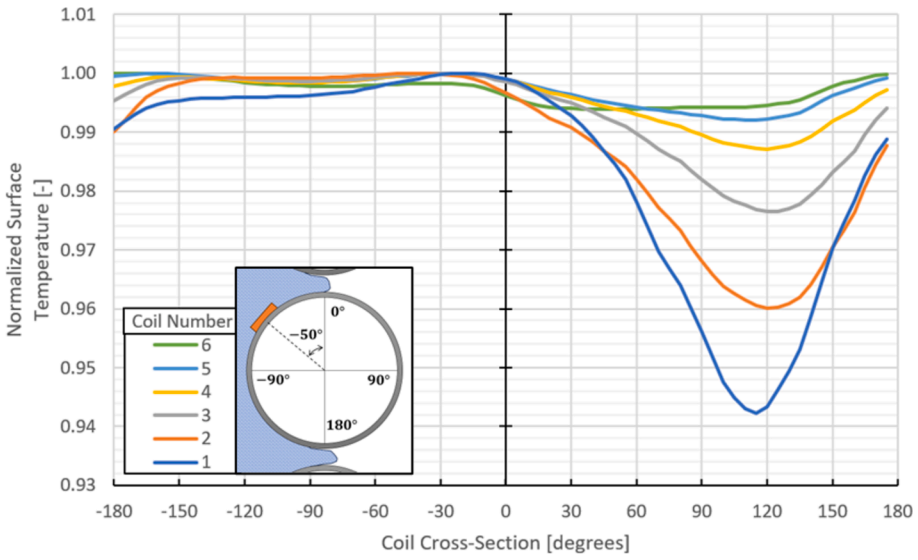

Fig. 12. Normalized coil surface temperature (in Kelvin) at the cross section of each coil turn according to CFD results of Craig et al. [16]. Coil turn 6.5 was assumed to have the same normalized temperature contour as coil turn 6.

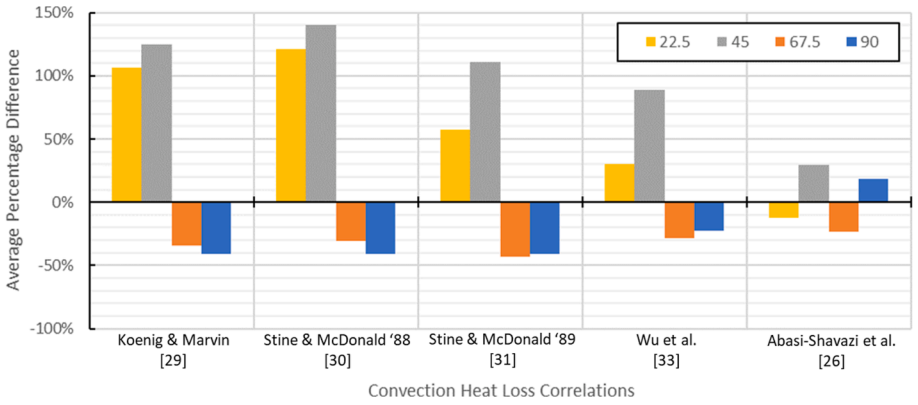

Fig. 13. Average percentage difference between the convection heat loss correlations and the experimental convection heat loss at various elevation angles. Natural convection heat loss correlations from literature are superimposed with forced convection heat loss of Ma [34].

open-cavity tubular receiver to be used in a solar-dish Brayton cycle. The total heat loss rate from the receiver was calculated from the inlet and outlet air temperature measurements and air mass flow measurements. Parametric control was exercised over elevation angles between 22.5° and 90°, average air mass flow rates between 33 g/s and 68 g/s and average inner-cavity temperatures up to 550 °C. Average ambient temperatures ranged from 13 °C to 22 °C and average wind speeds ranged from 0.5 m/s to 3.3 m/s. Radiation and conduction heat losses from the receiver were analytically determined from receiver surface temperature measurements. Convection heat loss was determined through an energy balance. Experiments were conducted for various air inlet temperatures and receiver elevation angles to characterize heat loss for the cavity receiver. The effect of the receiver elevation angle on total heat loss is not clearly visible for the elevation angles above 45° (9 % to 16 % increase compared to the total heat loss at the 90° elevation angle), but a 61 % increase in heat loss was observed for the elevation angle of 22.5°. Total heat loss ranged from 1237 W to 3066 W in the current study with maximum heat loss occurring at a 22.5° elevation angle. The steady-state, experimental, free-forced convection heat loss data were compared to empirical correlations in literature showing good agreement with an average percentage difference of 3 % for the natural convection heat loss correlation of Abbasi-Shavazi et al. [26] superimposed with the forced convection heat loss correlation of Ma [34]. The correlation of Abbasi-Shavazi et al. [26] had the unique ability of modelling a non-uniform heat flux along the inner cavity and showed good correlation with a broad range of receiver geometries and studies during development. The study therefore found that the experimental convection heat loss results of the open-cavity tubular receiver with a relatively large pipe diameter and wind skirt were in range of the values predicted by literature for relatively small tube diameters. The results of the study provide a mechanism to estimate convection heat loss during field operation from the large-coiled pipe cavity receiver with a known degree of accuracy. Future studies should focus on obtaining more data points from a specific wind direction to make a detailed comparison on the accuracy of the different correlations at the varying convection heat loss ranges.

CRediT authorship contribution statement

Jonathan K. Swanepoel: Writing – review & editing, Writing – original draft, Visualization, Validation, Project administration, Methodology, Investigation, Formal analysis, Data curation, Conceptualization. **Willem G. le Roux:** Conceptualization, Funding acquisition, Project administration, Resources, Supervision, Writing – original draft, Writing – review & editing. **Casey Roosendaal:** Writing – review & editing, Project administration, Methodology, Investigation, Formal

analysis, Data curation, Conceptualization. **Jacques Buys:** Writing – review & editing, Writing – original draft, Visualization, Methodology, Investigation, Formal analysis, Data curation, Conceptualization.

Declaration of competing interest

The authors declare that they have no known competing financial interests or personal relationships that could have appeared to influence the work reported in this paper.

Acknowledgements

The authors would like to acknowledge the financial support from the Technology Innovation Agency (TIA) of South Africa, and the Renewable Energy Hub and Spokes Programme of the Department of Science and Innovation (DSI) through the UP Solar Thermal Spoke.

Appendix A. Uncertainty analysis

An uncertainty analysis was conducted according to the standards outlined in ISO/IEC GUIDE 98-3:2008 [35]. Standard uncertainty refers to one standard deviation from the mean and expanded uncertainty refers to two standard deviations from the mean (95 % confidence interval). The relative uncertainty is determined by taking the expanded uncertainty over the reference value. The reference values were determined from a single data point. The data point with the maximum steady-state heat loss was chosen for the analysis. 3066 W total heat loss was the maximum reported in this study and it occurred for an average inner-cavity temperature of 469°C at a 22.5° elevation angle.

Table A1 summarises the results of the uncertainty analysis. The relative uncertainty for the steady-state total heat loss was determined to be 7 % while the relative uncertainties for conduction, radiation and convection heat losses were 1 %, 2 % and 13 %, respectively. The uncertainties for the averaged steady-state data are lower since each steady-state data point was averaged over 100 samples each.

Table A1
Summary of uncertainty analysis (example).

Summary	Units	Reference value	Standard uncertainty	Expanded uncertainty	Relative uncertainty
Sample data					
Air mass flow rate	kg/s	4.24E-02	1.72E-03	3.45E-03	8 %
Inlet pressure	Pa	88144.5	250.2	500.5	1 %
Outlet pressure	Pa	87100.0	167.4	334.9	0 %
Inlet corrected temperature	K	1099.3	1.2	2.5	0 %
Outlet corrected temperature	K	763.1	0.9	1.9	0 %
Cavity temperature	K	741.8	13.0	26.0	4 %
Insulation temperature	K	306.2	12.4	24.8	8 %
Total heat loss	W	2934.4	314.1	628.2	21 %
Conduction heat loss	W	424.6	23.0	46.0	11 %
Radiation heat loss	W	974.7	72.7	145.4	15 %
Convection heat loss	W	1535.0	323.2	646.5	42 %
5-minute average steady-state data					
Total heat loss (steady-state)	W	3066.3	104.4	208.8	7 %
Conduction heat loss	W	425.9	2.4	4.8	1 %
Radiation heat loss	W	975.7	7.5	14.9	2 %
Convection heat loss	W	1664.7	105.1	210.3	13 %

Appendix B. Steady-state tabulated data

The averaged 5-minute steady-state sample data captured during testing are tabulated and presented in this section. The relative averaged wind direction is given relative to the tracker azimuth. The positive range (<0° to 90°) defines a wind direction with a front-on wind component (a wind component incident with the receiver aperture), the negative range (−90° to <0°) defines a wind direction with a back-on wind component (a wind component incident with the back of the receiver). A 0° relative wind direction is a pure side-on wind (parallel to the aperture plane). Tables B1 to B4 present the averaged measured values for the entire range of elevation angles. The sample numbers in the first column of Tables B1 to B4 respectively correlate with the sample numbers in Tables 3 to 6. The average outer-cavity temperature was determined for the average of the surface thermocouple measurement on the outer coil (contacting the insulation board). The average inner-cavity temperature was determined from the average of the 6.5 coil surface temperatures exposed to the inner cavity (determined using Table 2) and the top insulation temperature exposed to the inner cavity.

Table B1
90° elevation angle steady-state data points averaged over 5 min. Cavity temperature is averaged over all coil turns in the cavity and temperature ratios are determined from temperatures in Kelvin.

Sample	**Date (dd mm)**	$\dot{m}$ **(g/s)**	***WS*** **(m/s)**	***WD*** **(deg)**	T_{amb} **(°C)**	P_{amb} **(kPa)**	$T_{cav,outer}$ **(°C)**	$T_{cav,inner}$ **(°C)**	$\frac{T_{cav,inner}}{T_{cav,outer}}$	$\frac{T_6}{T_5}$
1	19 07	45	1.5	−51	14	87	420	408	98 %	99 %
2	19 07	49	1.0	10	16	87	423	412	98 %	99 %
3	19 07	33	1.4	28	14	87	409	398	98 %	99 %
4	19 07	62	1.7	−28	14	87	424	413	98 %	99 %

(*continued on next page*)

Table B1 (*continued*)

Sample	Date (dd mm)	$\dot{m}$ (g/s)	WS (m/s)	WD (deg)	T_{amb} (°C)	P_{amb} (kPa)	$T_{cav,outer}$ (°C)	$T_{cav,inner}$ (°C)	$\frac{T_{cav,inner}}{T_{cav,outer}}$	$\frac{T_6}{T_5}$
5	02 07	41	1.6	−52	21	87	509	496	98 %	99 %
6	20 10	51	2.0	−4	20	87	464	452	98 %	99 %
7	02 07	49	1.6	−2	19	87	516	503	98 %	99 %
8	02 07	50	2.1	−7	21	87	514	502	98 %	99 %
9	02 07	39	1.5	57	17	87	503	490	98 %	99 %
10	02 06	53	3.0	−84	17	86	566	553	98 %	99 %
11	08 07	42	0.5	13	15	87	551	537	98 %	99 %
12	02 06	40	2.0	−31	15	86	545	531	98 %	99 %

Table B2
67.5° elevation angle steady-state data points averaged over 5 min. Cavity temperature is averaged over all coil turns in the cavity and temperature ratios are determined from temperatures in Kelvin.

Sample	Date (dd mm)	$\dot{m}$ (g/s)	WS (m/s)	WD (deg)	T_{amb} (°C)	P_{amb} (kPa)	$T_{cav,outer}$ (°C)	$T_{cav,inner}$ (°C)	$\frac{T_{cav,inner}}{T_{cav,outer}}$	$\frac{T_6}{T_5}$
1	08 07	41	1.3	−10	15	87	508	496	98 %	99 %
2	20 10	51	1.7	25	21	87	462	450	98 %	99 %
3	31 08	39	2.7	−57	21	86	539	522	98 %	99 %
4	31 08	39	2.8	−57	21	86	539	525	98 %	99 %
5	26 07	42	1.0	46	14	87	538	524	98 %	99 %

Table B3
45° elevation angle steady-state data points averaged over 5 min. Cavity temperature is averaged over all coil turns in the cavity and temperature ratios are determined from temperatures in Kelvin.

Sample	Date (dd mm)	$\dot{m}$ (g/s)	WS (m/s)	WD (deg)	T_{amb} (°C)	P_{amb} (kPa)	$T_{cav,outer}$ (°C)	$T_{cav,inner}$ (°C)	$\frac{T_{cav,inner}}{T_{cav,outer}}$	$\frac{T_6}{T_5}$
1	17 06	41	1.6	–32	19	87	509	497	98 %	99 %
2	17 06	49	2.1	−7	21	87	514	501	98 %	99 %
3	21 10	41	2.7	81	21	87	449	437	98 %	98 %
4	17 06	50	1.9	39	21	87	512	500	98 %	99 %
5	17 06	52	2.1	−13	21	87	511	499	98 %	99 %
6	17 06	68	1.8	−45	22	87	520	507	98 %	99 %
7	15 06	41	2.0	17	19	87	553	540	98 %	98 %
8	15 06	62	1.0	57	20	87	559	546	98 %	99 %
9	15 06	52	2.6	51	19	87	553	540	98 %	98 %

Table B4
22.5° elevation angle steady-state data points averaged over 5 min. Cavity temperature is averaged over all coil turns in the cavity and temperature ratios are determined from temperatures in Kelvin.

Sample	Date (dd mm)	$\dot{m}$ (g/s)	WS (m/s)	WD (deg)	T_{amb} (°C)	P_{amb} (kPa)	$T_{cav,outer}$ (°C)	$T_{cav,inner}$ (°C)	$\frac{T_{cav,inner}}{T_{cav,outer}}$	$\frac{T_6}{T_5}$
1	21 10	41	1.8	−18	19	87	445	432	98 %	98 %
2	21 10	52	1.1	−2	20	87	456	443	98 %	98 %
3	21 10	52	2.9	33	21	87	457	445	98 %	98 %
4	27 07	54	3.4	–22	14	87	496	483	98 %	98 %
5	27 07	43	1.8	38	13	87	483	469	98 %	98 %

References

[1] W. Lipiński, et al., Progress in heat transfer research for high-temperature solar thermal applications, *Appl. Therm. Eng.* 184 (2021) 116137, https://doi.org/10.1016/j.applthermaleng.2020.116137.

[2] S.Y. Wu, L. Xiao, Y. Cao, Y.R. Li, Convection heat loss from cavity receiver in parabolic dish solar thermal power system: a review, *Sol. Energy* 84 (8) (2010) 1342–1355.

[3] A. Steinfeld, M. Schubnell, Optimum aperture size and operating temperature of a solar cavity-receiver, *Sol. Energy* 50 (1) (1993) 19–25, https://doi.org/10.1016/0038-092X(93)90004-8.

[4] J.A. Harris, T.G. Lenz, Thermal performance of solar concentrator/cavity receiver systems, *Sol. Energy* 34 (2) (1985) 135–142, https://doi.org/10.1016/0038-092X(85)90170-7.

[5] L. Xiao, S. He, S.Y. Wu, Z.L. Chen, Optical-thermal conversion characteristics of cylindrical receiver with built-in helically coiled tubes, *Sustainable Energy Technol. Assess.* 37 (2020).

[6] W.G. Le Roux, T. Bello-Ochende, J.P. Meyer, The efficiency of an open-cavity tubular solar receiver for a small-scale solar thermal Brayton cycle, *Energy Convers. Manage.* 84 (2014) 457–470, https://doi.org/10.1016/j.enconman.2014.04.048.

[7] R.D. Jilte, S.B. Kedare, J.K. Nayak, Investigation on convective heat losses from solar cavities under wind conditions, *Energy Procedia* 57 (2014) 437–446, https://doi.org/10.1016/j.egypro.2014.10.197.

[8] A.M. Daboo, S. Mahmoud, R.K. Al-Dadah, The optical efficiency of three different geometries of a small scale cavity receiver for concentrated solar applications, *Appl. Energy* 179 (2016) 1081–1096, https://doi.org/10.1016/j.apenergy.2016.07.064.

[9] M. Prakash, S.B. Kedare, J.K. Nayak, Investigations on heat losses from a solar cavity receiver, *Sol. Energy* 83 (2009) 157–170.

[10] J. Zhu, K. Wang, H. Wu, D. Wang, J. Du, A.G. Olabi, Experimental investigation on the energy and exergy performance of a coiled tube solar receiver, *Appl. Energy* 156 (2015) 519–527, https://doi.org/10.1016/j.apenergy.2015.07.013.
[11] K. Wang, et al., Experimental study on a coiled tube solar receiver under variable solar radiation condition, *Sol. Energy* 122 (2015) 1080–1090, https://doi.org/10.1016/j.solener.2015.10.004.
[12] W.G. Le Roux, T. Bello-Ochende, J.P. Meyer, Optimisation of an open rectangular cavity receiver and recuperator used in a small-scale solar thermal Brayton cycle with thermal losses, 10th, International Conference on Heat Transfer, Fluid Mechanics and Thermodynamics (HEFAT2014), (July, 2014).
[13] W.G. Le Roux, Thermodynamic optimisation and experimental collector of a dish-mounted small-scale solar thermal Brayton cycle, University of Pretoria, Pretoria, South Africa, 2015. PhD Thesis.
[14] T.M. Wolff, "Initial testing of a collector for a solar-dish Brayton cycle," MEng Dissertation, University of Pretoria, Pretoria, 2022.
[15] T.M. Wolff, W.G. Le Roux, J.P. Meyer, "Heat loss analysis for an open-cavity tubular solar receiver," 16th International Heat Transfer Conference (IHTC-16), Beijing, China, 10-15 August, 2018. https://doi.org/10.1615/IHTC16.nee.024010.
[16] K.J. Craig, M. Slootweg, W.G. Le Roux, T.M. Wolff, J.P. Meyer, Using CFD and ray tracing to estimate the heat losses of a tubular cavity dish receiver for different inclination angles, *Sol. Energy* 211 (2020) 1137–1158, https://doi.org/10.1016/j.solener.2020.10.054.
[17] C. Roosendaal, J.K. Swanepoel, W.G. Le Roux, Performance analysis of a novel solar concentrator using lunar flux mapping techniques, *Sol. Energy* 206 (2020) 200–215, https://doi.org/10.1016/j.solener.2020.05.050.
[18] Refraline (Pty) Ltd. *Ceramic fibre board*, [Data Sheet]. Refraline, Germiston, South Africa. [Online]. Available: www.refraline.com.
[19] SUTO iTEC, "Instruction and operation manual S421 thermal mass flow sensor." [Online]. Available: www.suto-itec.com.
[20] NAVIS Elektronika. "NAVIS anemometers." www.navis-anemometers.com/ (accessed 20 March, 2023).
[21] I.H. Bell, J. Wronski, S. Quoilin, V. Lemort, Pure and pseudo-pure fluid thermophysical property evaluation and the open-source thermophysical property library CoolProp, *Ind. Eng. Chem. Res.* 53 (6) (2014) 2498–2508, https://doi.org/10.1021/ie4033999.
[22] Y.A. Çengel, A.J. Ghajar, *Heat and Mass Transfer: Fundamentals and Applications*, 5th ed., McGraw-Hill Education, New York, NY, United States, 2014.
[23] R.H. Bogaard, P.D. Desai, H.H. Li, C.Y. Ho, Thermophysical properties of stainless steels, *Thermochim Acta* 218 (1993) 373–393, https://doi.org/10.1016/0040-6031(93)80437-F.
[24] S.W. Churchill, M. Bernstein, A correlating equation for forced convection from gases and liquids to a circular cylinder in crossflow, *ASME J. Heat Transfer* 99 (2) (1977) 300–306, https://doi.org/10.1115/1.3450685.
[25] J.K. Swanepoel, W.G. Le Roux, A.S. Lexmond, J.P. Meyer, Helically coiled solar cavity receiver for micro-scale direct steam generation, *Appl. Therm. Eng.* 185 (2021) 116427, https://doi.org/10.1016/j.applthermaleng.2020.116427.
[26] E. Abbasi-Shavazi, J.F. Torres, G. Hughes, J. Pye, Experimental correlation of natural convection losses from a scale-model solar cavity receiver with non-isothermal surface temperature distribution, *Sol. Energy* 198 (2020) 355–375, https://doi.org/10.1016/j.solener.2020.01.023.
[27] C.G. McDonald, "Heat loss from an open cavity," Sandia National Laboratories, Albuquerque (NM), United States, SAND95-2939, 1995. [Online]. Available: https://doi.org/10.2172/188598.
[28] M.J. Brooks, et al., SAURAN: a new resource for solar radiometric data in Southern Africa [Online]. Available: *J. Energy Southern Africa* 26 (1) (2015) 2–10 https://www.scielo.org.za.
[29] A.A. Koenig, M. Marvin, "Convection heat loss sensitivity in open cavity solar receivers. Final Report," Department of Energy (DOE) Oak Ridge (TN), United States, EG77-C-04-3985, 1981.
[30] W.B. Stine, C.G. McDonald, "Cavity receiver heat loss measurements," in *10th Annual ASME Solar Energy Conference*, Denver (CO), United States, 10-14 April 1988: American Society of Mechanical Engineers (ASME), 1988.
[31] W.B. Stine, G.G. McDonald, "Cavity receiver convection heat loss," in *Proceedings of the International Solar Energy Society. Solar World Congress*, Kobe, Japan, 4-8 September 1989, vol. 1318: International Solar Energy Society (ISES), 1989.
[32] D.L. Siebers, J.S. Kraabel, "Estimating convective energy losses from solar central receivers," Sandia National Laboratories, Albuquerque (NM), United States, SAND-84-8717, 1984. [Online]. Available: https://doi.org/10.2172/6906848.
[33] S.Y. Wu, L. Xiao, Y.R. Li, Effect of aperture position and size on natural convection heat loss of a solar heat-pipe receiver, *Appl. Therm. Eng.* 31 (2011) 2787–2796, https://doi.org/10.1016/j.applthermaleng.2011.05.004.
[34] R.Y. Ma, "Wind effects on convective heat loss from a cavity receiver for a parabolic concentrating solar collector," Sandia National Laboratories, Albuquerque (NM), United States, SAND-92-7293, 1993. [Online]. Available: https://doi.org/10.2172/10192244.
[35] *ISO Guide 98-3:2008, Uncertainty of measurement-Part 3: Guide to the expression of uncertainty in measurement*, International Organization for Standardisation, Geneva, Switzerland, 2008.